Durham Research Online

Deposited in DRO:

22 June 2016

Version of attached file:

Published Version

Peer-review status of attached file:

Peer-reviewed

Citation for published item:

Shidatsu, M. and Ueda, Y. and Yamada, S. and Done, C. and Hori, T. and Yamaoka, K. and Kubota, A. and Nagayama, T. and Moritani, Y. (2014) 'Spectral and timing properties of the black hole X-ray binary H1743-322 in the low/hard state studied with Suzaku.', Astrophysical journal., 789 (2). p. 100.

Further information on publisher's website:

http://dx.doi.org/10.1088/0004-637X/789/2/100

Publisher's copyright statement:

Additional information:

SPECTRAL AND TIMING PROPERTIES OF THE BLACK HOLE X-RAY BINARY H1743−322 IN THE LOW/HARD STATE STUDIED WITH *SUZAKU*

M. SHIDATSU[1], Y. UEDA[1], S. YAMADA[2], C. DONE[3], T. HORI[1], K. YAMAOKA[4], A. KUBOTA[5], T. NAGAYAMA[6], AND Y. MORITANI[7]

[1] Department of Astronomy, Kyoto University, Kitashirakawa-Oiwake-cho, Sakyo-ku, Kyoto 606-8502, Japan; shidatsu@kusastro.kyoto-u.ac.jp
[2] Department of Physics, Tokyo Metropolitan University, Minami-Osawa 1-1, Hachioji, Tokyo 192-0397, Japan
[3] Department of Physics, University of Durham, South Road, Durham, DH1 3LE, UK
[4] Solar-Terrestrial Environment Laboratory, Nagoya University, Furo-cho, Chikusa-ku, Nagoya, Aichi 464-8601, Japan
[5] Department of Electronic Information Systems, Shibaura Institute of Technology, 307 Fukasaku, Minuma-ku, Saitama 337-8570, Japan
[6] Department of Physics, Faculty of Science, Kagoshima University, 1-21-35 Korimoto, Kagoshima 890-0065, Japan
[7] Department of Physical Sciences, Hiroshima University, Higashi-Hiroshima, Hiroshima 739-8526, Japan

ABSTRACT

We report on the results from *Suzaku* observations of the Galactic black hole X-ray binary H1743−322 in the low/hard state during its outburst in 2012 October. We appropriately take into account the effects of dust scattering to accurately analyze the X-ray spectra. The time-averaged spectra in the 1–200 keV band are dominated by a hard power-law component of a photon index of ≈1.6 with a high-energy cutoff at ≈60 keV, which is well described with the Comptonization of the disk emission by the hot corona. We estimate the inner disk radius from the multi-color disk component, and find that it is 1.3–2.3 times larger than the radius in the high/soft state. This suggests that the standard disk was not extended to the innermost stable circular orbit. A reflection component from the disk is detected with $R = \Omega/2\pi \approx 0.6$ (Ω is the solid angle). We also successfully estimate the stable disk component independent of the time-averaged spectral modeling by analyzing short-term spectral variability on a ∼1 s timescale. A weak low-frequency quasi-periodic oscillation at 0.1–0.2 Hz is detected, whose frequency is found to correlate with the X-ray luminosity and photon index. This result may be explained by the evolution of the disk truncation radius.

Key words: accretion, accretion disks – black hole physics – X-rays: binaries – X-rays: individual (H1743−322)

Online-only material: color figures

1. INTRODUCTION

A large fraction of known Galactic black hole X-ray binaries (BHXBs) are highly transient sources. They are thought to be low-mass X-ray binaries, in which a stellar mass black hole accretes gas from a low-mass donor star via Roche-lobe overflow. They normally stay in a very faint state, but occasionally undergo dramatic outbursts, changing their X-ray luminosities by several orders of magnitude (e.g., Tanaka & Shibazaki 1996) on a human timescale (typically ≈10 days to several months for the entire period of an outburst). Thus, they are excellent targets to study the physics of black hole accretion over a wide range of mass accretion rates. Along with the increase and decrease of the X-ray luminosity, they exhibit several distinct "states" with different spectral and timing properties. The most canonical ones among them are the so-called high/soft state and the low/hard state, which appears in relatively high and low luminosities ($\sim 0.1 L_{\rm Edd}$,[8] and $\lesssim 10^{-2} L_{\rm Edd}$, respectively; see, e.g., McClintock & Remillard 2006; Done et al. 2007 for a review).

In the high/soft state, the X-ray flux is dominated by the thermal emission from the optically thick and geometrically thin accretion disk (the standard disk; Shakura & Sunyaev 1973), and the observed spectrum is well reproduced with a multi-color disk model (Mitsuda et al. 1984). The inner disk radius stays constant during the high/soft state, regardless of the significant change in X-ray luminosity (e.g., Ebisawa et al. 1993; Kubota

& Makishima 2004; Steiner et al. 2010; Shidatsu et al. 2011a). This indicates that the standard disk stably extends down to the innermost stable circular orbit (ISCO). In the low/hard state, BHXBs exhibit a hard, power-law-shaped X-ray spectrum with a photon index of <2 and an exponential cutoff at ≈100 keV. This spectral shape is generally described as unsaturated Compton scattering of the soft X-ray photons from the accretion disk by thermal electrons in hot inner flow or corona. Previous studies suggested that the standard disk is truncated in the low/hard state and eventually extends inward according to the increase of X-ray luminosity (Tomsick et al. 2009; Shidatsu et al. 2011b; Yamada et al. 2013; Kolehmainen et al. 2014). However, in what luminosity the standard disk reaches the ISCO is still controversial. Further study is necessary to fully understand the inner disk structure and its evolution in response to the change in mass accretion rate in the low/hard state.

The fast time variability of BHXBs provides clues to the structure of the inner accretion disk and corona. In the low/hard state, the power density spectra (PDSs) are roughly described by a strong band-limited noise component, a flat-topped spectrum in the νP_ν form between the low- and high-frequency breaks. The low-frequency break moves to higher frequencies according to the rapid rise of the X-ray flux. This suggests that the break is associated with the truncation radius of the standard disk (Ingram & Done 2012). Extracting the energy spectra of the noise component, Axelsson et al. (2005) found that the fast variability is produced by Comptonized emission from the vicinity of the black hole. Quasi-periodic oscillations (QPOs) are sometimes detected on the band-limited noise. Previous studies reported that the observed QPO frequencies are correlated with the spectral index and disk flux (e.g.,

---

[8] $L_{\rm Edd}$ is the Eddington luminosity: $4\pi G m_{\rm p} c M_{\rm BH}/\sigma_{\rm T}$, where G, $m_{\rm p}$, c, $M_{\rm BH}$, and $\sigma_{\rm T}$ represent the gravitational constant, proton mass, speed of light, black hole mass, and Thomson scattering cross-section, respectively.

Table 1
Log of the *Suzaku* Observations

	Epoch 1	Epoch 2	Epoch 3
ObsID	407005010	407005020	407005030
Start time (UT)	2012 Oct 4 18:46:29	2012 Oct 10 15:30:34	2012 Oct 12 09:43:11
End time (UT)	2012 Oct 5 14:35:16	2012 Oct 11 14:04:14	2012 Oct 13. 08:59:13
XIS window	1/4	1/4	1/4
Burst option	1.0 s	1.0 s	1.0 s
Net exposure			
XIS	21 ks	21 ks	21 ks
HXD	42 ks	42 ks	43 ks

Sobczak et al. 2000; Titarchuk & Fiorito 2004; Shaposhnikov & Titarchuk 2007), implying that the QPOs, as well as the band-limited noise, are coupled with the inner disk structure.

H1743−322 is a transient BHXB discovered by *Ariel-V* in 1977 (Kaluzienski & Holt 1977). Since then, it has displayed more than 10 outbursts, which were extensively observed by X-ray satellites. This source exhibits outbursts recurrently with an interval of ≈200 days (Shidatsu et al. 2012). Some of them were "failed" outbursts, in which the high/soft state is missing (e.g., Capitanio et al. 2009; Chen et al. 2010). High- and low-frequency QPOs (LF QPOs) were detected above 100 Hz and below 10 Hz in many observations (e.g., Homan et al. 2003, 2005; Tomsick & Kalemci 2003). The X-ray spectra of H1743−322 were also obtained many times in various states, including wide-band data up to ∼100 keV taken with *INTEGRAL* and *Suzaku* (Capitanio et al. 2005; Blum et al. 2010). Ionized absorption lines, likely originating from disk winds, were discovered in the high/soft state and the steep power-law (or "very high") state in *Chandra* high-resolution spectra (Miller et al. 2006). This suggests that the source has a high inclination angle.

H1743−322 was also observed in other wavelengths. Optical and near-infrared counterparts were identified by Steeghs et al. (2003) and Baba et al. (2003), respectively. However, the high Galactic extinction has hampered deeper monitoring observations to dynamically measure the black hole mass. Bright radio flares likely associated with relativistic jets were detected in the early phase of the outbursts (e.g., Rupen et al. 2003). In the 2003 outburst, bipolar large-scale X-ray jets were resolved with *Chandra* (Corbel et al. 2005). Combining the *Chandra* image with the radio data obtained with the very Large Array (VLA) during the same outburst, Steiner et al. (2012) estimated the distance, the inclination angle, and the spin parameter a of the black hole ($a = cJ/GM_{BH}^2$, where J represents the angular momentum) as 8.5 ± 0.8 kpc, $75° \pm 3°$, and 0.2 ± 0.3, respectively. They were derived by modeling the trajectories of the bipolar jets with a symmetric kinematic model.

On 2012 September 24, the brightening of H1743−322 was reported by Shidatsu et al. (2012) with the *Monitor of All-sky X-ray Image* (*MAXI*; Matsuoka et al. 2009)/Gas Slit Camera (GSC; Mihara et al. 2011). About two weeks later, we triggered three sequential Target-of-Opportunity (ToO) observations with *Suzaku* (Mitsuda et al. 2007), when the X-ray flux reached the peak and started decreasing. Quasi-simultaneous observations in the near-infrared (J, H, and K_S) and optical (R and i) bands were also carried out with the *Infrared Survey Facility* (*IRSF*) 1.4 m telescope and the *Kanata* 1.5 m telescope at Higashi-Hiroshima Observatory, respectively. The source was not detected in any bands, however.

In this paper, we report the results of spectral and timing studies using the *Suzaku* data sets. Section 2 describes the

details of the *Suzaku* observations and the data reduction. In Section 3, we present the *Suzaku* light curves and power spectra. The spectral analysis and the results are described in Section 4. The infrared and optical observations are summarized in Section 5. Section 6 discusses the *Suzaku* results and Section 7 presents the summary and conclusions. Errors represent the 90% confidence range for a single parameter of interest, unless otherwise specified. Throughout the article, we refer to the table by Anders & Grevesse (1989) as the solar abundances. We assume the distance and inclination of H1743−322 as those determined by Steiner et al. (2012), $D = 8.5$ kpc and $i = 75°$.

2. *SUZAKU* OBSERVATIONS AND DATA REDUCTION

Suzaku ToO observations of H1743−322 were performed on 2012 October 4, 10, and 12, with a net exposure of ≈40 ks in each epoch. Figure 1 plots the long-term X-ray light curves of the *MAXI*/GSC and the *Swift*/Burst Alert Telescope (BAT; Barthelmy et al. 2005) and their hardness ratio, in which the *Suzaku* epochs are marked with shaded regions. The first observation (hereafter "Epoch 1") is close to the peak of the BAT hard X-ray flux in the 15–50 keV band and the second and third observations ("Epoch 2" and "Epoch 3," respectively) are in the decaying phase, where the fluxes are lower than that of Epoch 1 by ≈20%.

Suzaku carries three currently available X-ray charge-coupled-device (CCD) cameras called the X-ray Imaging Spectrometer (XIS), which detects X-ray photons of 0.2–12 keV, and a hard X-ray sensor called the Hard X-ray Detector (HXD) composed of silicon PIN diodes and GSO scintillators covering the 10–70 keV and 40–600 keV bands, respectively. The XIS consists of frontside-illuminated cameras (FI-XISs; XIS-0 and XIS-3) and a backside-illuminated camera (BI-XIS; XIS-1), which is more sensitive to soft X-rays below ≈1.5 keV than FI-XISs. In our observations, the 1/4 window mode and the 1.0 s burst option were employed for both FI- and BI-XISs to avoid pile-up effects. A summary of the *Suzaku* observations is given in Table 1.

We utilized HEAsoft 6.13 and *Suzaku* Calibration Database (CALDB) released on 2013 March 5 for the reduction and analysis of our data. We started with the "cleaned" events (whose process version is 2.8.16.34) provided by the *Suzaku* team and followed the standard procedure for the data reduction. Source photons were extracted from a circular region with a radius of 110″ centering at the target position. Background events were collected within a circle with a radius of 120″ taken in a blank sky area outside of the region for source extraction. The XIS response matrix and ancillary response files were generated by `xisrmfgen` and `xissimarfgen` (Ishisaki et al. 2007), respectively. The non-X-ray background (NXB) was subtracted from the HXD data using the modeled NXB
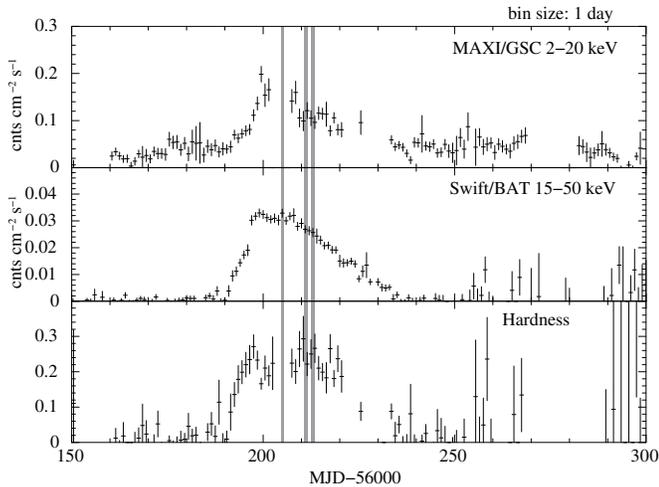
Figure 1. Long-term light curves of H1743−322 in the 2–20 keV band obtained with *MAXI*/GSC (top) and in the 15–50 keV band from *Swift*/BAT (middle), and the hardness ratio calculated from these two light curves (bottom). The shaded regions indicate the *Suzaku* observations. MJD 56201 corresponds to 2012 October 1.
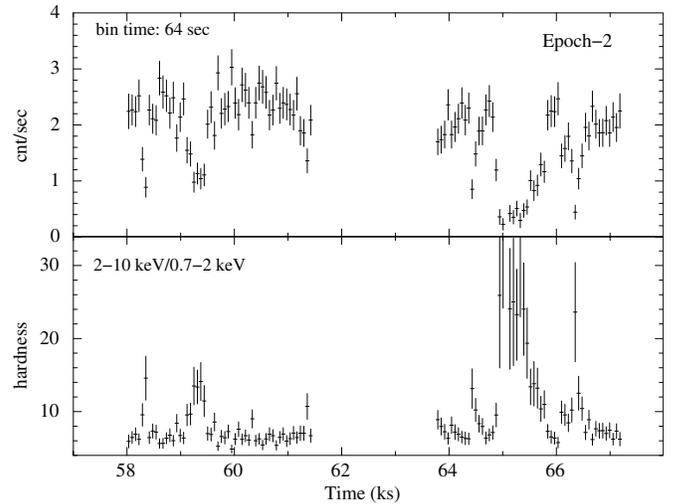

Figure 3. *Suzaku* light curve and hardness ratio in Epoch 2 focused on the dipping periods. Top: the XIS-0 light curve in the 0.7–2 keV band binned in 64 s. Bottom: the hardness ratio between the 2–10 keV and 0.7–2 keV bands. Similar hardening can also be seen in the dipping period of Epoch 3.

files produced by the HXD team.[9] In the spectral analysis, `ae_hxd_pinxinome11_20110601.rsp` was used as the response file for PIN, and `ae_hxd_gsoxinom_20100524.rsp` and `ae_hxd_gsoxinom_crab_20100526.arf` were used for GSO.

Because H1743−322 is located in a crowded region close to the center of our Galaxy ($l, b = 357°.26, −1°.83$), the HXD spectra could be contaminated with the Galactic diffuse X-ray background (GXB) and nearby bright point sources. However, we find that the GXB contributes only ≈1.5% of the total flux in the PIN bandpass, and far less than that in the GSO bandpass, which are negligible. To estimate these values, we assumed the GXB spectrum at $(l, b) = (28°.5, 0°.2)$ shown in Kubota et al. (2010) and converted the fluxes in the PIN and GSO energy ranges to those at the position of H1743−322 using the spatial profile of the GXB in the 16–70 keV band obtained with *INTEGRAL*/IBIS (Krivonos et al. 2007). The cosmic

X-ray background (CXB) is not subtracted from the HXD data because its contribution is even smaller than that of the GXB. We examined the contamination of nearby sources using the *Swift*/BAT 70 month catalog (Baumgartner et al. 2013), considering the detector's transmission functions (Takahashi et al. 2007). We also checked the variability of the sources through the *MAXI*/GSC and *Swift*/BAT public light curves. The nearby sources were found to contribute only <1% and ≈1% of the observed PIN and GSO fluxes, respectively, both of which are ignorable.

3. X-RAY LIGHT CURVES AND TIMING PROPERTIES

Figure 2 presents the *Suzaku* light curves in the three epochs. They sometimes display significant drops of the soft X-ray flux in Epoch 2 and Epoch 3. These are likely "absorption dips," which are thought to be caused by the obscuration of the central X-ray source by the outer edge of the accretion disk hit by the accretion stream from the companion star. As noted in Figure 3, the hardness ratio increases in these dipping periods. This indicates that the dips are caused by photo-electric
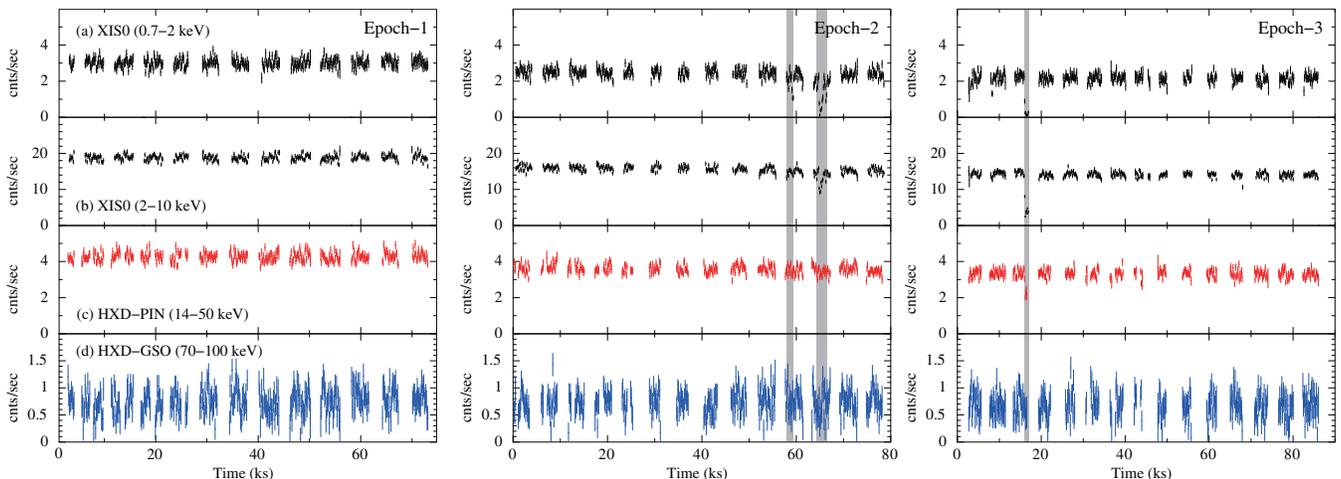
---

[9] http://www.astro.isas.ac.jp/suzaku/analysis/hxd/pinnxb/tuned/ for PIN and http://www.astro.isas.ac.jp/suzaku/analysis/hxd/gsonxb/ for GSO

Figure 2. *Suzaku* XIS and HXD light curves of Epoch 1 (left), Epoch 2 (middle), and Epoch 3 (right). The shaded regions are dipping periods.
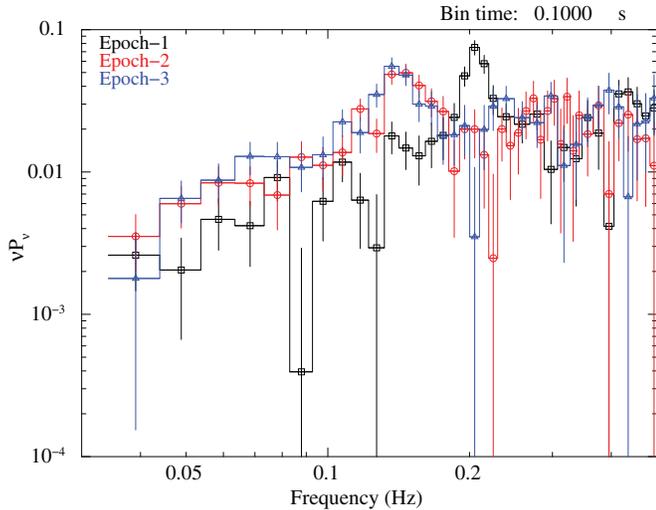(A color version of this figure is available in the online journal.)

Figure 4. Normalized power density spectra (PDSs) in the three epochs created from the PIN light curves with 0.1 s bins. They are normalized in such a way that their integral gives the squared root mean squared fractional variability. White noise is subtracted from all PDSs.

(A color version of this figure is available in the online journal.)

Figure 5. Time-averaged spectra in Epoch 1 (black, filled square), Epoch 2 (red, open circle), and Epoch 3 (blue, cross). The spectral ratios of Epoch 2 and Epoch 3 with respect to Epoch 1 are plotted in the lower panel.

(A color version of this figure is available in the online journal.)

absorption, although the dipping duration is too short and does not allow us to perform precise time-resolved spectral analysis. The presence of similar absorption dips in H1743−322 was also reported in previous observations (e.g., Homan et al. 2005). We define the shadowed regions in Figure 2 as the dipping periods, in which the count rate in the 0.7–2 keV band is ≳30% smaller than the averaged rate in the individual epochs, and exclude them in the following analysis.

Figure 4 plots the normalized PDSs in the three epochs obtained with the PIN data. The PDSs are dominated by a strong noise components with a normalized power of ≈10^{-2} (rms/mean)^2 in the νP_ν form, consistent with those of typical BHXBs in the low/hard state (see e.g., McClintock & Remillard 2006). A weak LF QPO is also detected in each epoch. Fitting it with a Gaussian model, we estimate the central frequency of the QPO as 0.206 ± 0.003 Hz in Epoch 1, which becomes 1.4 times lower in Epoch 2 and Epoch 3 (0.147 ± 0.004 Hz and 0.141 ± 0.004 Hz, respectively) as the *Swift*/BAT flux is decreased by ≈20%. This QPO is detected in the XIS PDSs as well.

4. ANALYSIS OF *SUZAKU* SPECTRA

We create the time-averaged spectra of the three epochs and analyze them separately on XSPEC version 12.8.0. Considering the signal-to-noise ratio and the reliability of the calibration, we use the data within 1–9 keV, 1–8 keV, and 14–70 keV for FI-XISs, BI-XIS, and PIN, respectively. For the GSO data, we only consider the 50–130 keV (Epoch 1), 50–220 keV (Epoch 2), and 50–200 keV (Epoch 3) bands, above which the signal levels are overcome by the systematic errors in the simulated background (≲1% of the total count rate; Fukazawa et al. 2009). The spectra and responses of FI-XISs (i.e., XIS-0 and XIS-3) are combined to improve statistics. The XIS data of 1.7–1.9 keV are discarded to avoid the uncertainties in the responses at energies around the complex instrumental Si–K edge. To account for possible calibration uncertainties, we add a 1% systematic error to every spectral bin in the XIS and HXD data, following Makishima et al. (2008). We find that the final best-fit parameters are the same within their 90% confidence ranges even if we assign 0%,
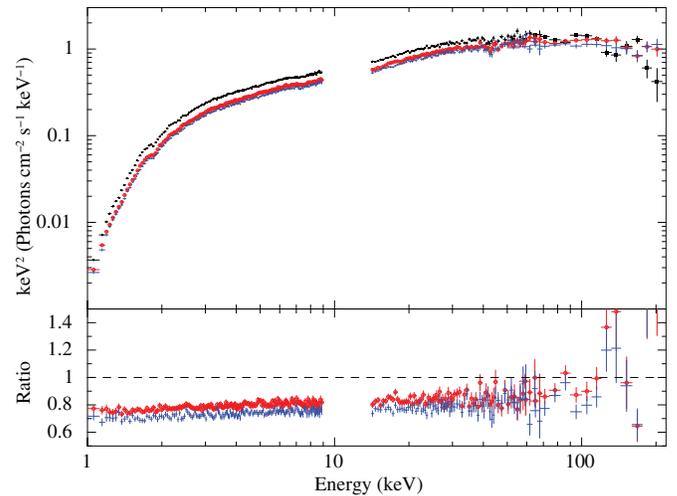
2%, and 3% systematic errors, and that the confidence ranges themselves are increased only by ≲10% from the case of 0% systematic error to that of 3%. We confirm that the conclusions are not affected. The cross-normalization of the HXD with respect to FI-XISs was fixed at 1.16,[10] while that of BI-XIS is left free. We examine the pileup effects in the XIS data using the software `aepileupcheckup.py`, which estimates the pileup fraction at various radii from the center of the XIS point-spread function (PSF; Yamada et al. 2012). We find that the pileup fraction is negligibly small in all observations, less than 2% even at the cores of the PSFs. Figure 5 shows the time-averaged spectra for the three epochs in the νF_ν form.

4.1. Dust-scattering Effects

In observations of heavily absorbed sources (with $N_H \gtrsim 10^{22}$ cm^{-2}), it must be borne in mind that dust scattering in addition to photo-electric absorption can significantly affect the observed soft X-ray spectra (Ueda et al. 2010; Hori et al. 2014). Diffuse interstellar (and circumbinary) dust can scatter out the X-ray photons from the line of sight and, at the same time, scatter in the photons emitted in different directions. Consequently, we see a "dust halo" around a point source. A dust halo was indeed resolved in GX 13 + 1 (Smith et al. 2002), which has almost the same column density ($N_H \approx 2 \times 10^{22}$ cm^{-2}) as our target. When we use data that do not fully cover the dust halo, those two scattering effects are not canceled out. In this case, the observed spectra, particularly in the soft X-ray band, are different from what we would expect if there were no dust scattering. This must be taken into account for accurate spectral modeling. Even if all the scattered photons are collected, the scattered-in and scattered-out components no longer compensate each other in variable sources due to the difference in arrival time between the scattered photons and those taking the straight path to the observer. In our case, the typical delay time of the scattered photons in the extraction region for the XIS is estimated to be ~1.3 days, by assuming a distance of 8.5 kpc. We confirm for all the *Suzaku* epochs that the flux variability of H1743−322

---

[10] http://www.astro.isas.ac.jp/suzaku/doc/suzakumemo/suzakumemo-2008-06.pdf

on that timescale is low enough to ignore the variability of the scattered-in component, as in the case of Hori et al. (2014).

Following Ueda et al. (2010) and Hori et al. (2014), we utilize Dscat, a local multiplicative model implemented in XSPEC, to account for the effects of dust scattering in the spectral analysis. Dscat estimates both scattering-in and -out components from the scattering fraction (the fraction of the scattered-in photons included in the data) and the hydrogen column density, by assuming the dust scattering cross section for $R_{\rm V} = 3.1$ calculated by Drain (2003). We fix the scattering fraction at 1.0 (i.e., all the scattered photons are included) for the HXD, which has a sufficiently large field of view to cover the whole dust halo. For the XIS, we adopt the same value (0.65) as Hori et al. (2014), because we used the same region as theirs to extract the source photons from the XIS data. In the following analysis, the column density of the Dscat model is always linked to that of the interstellar photo-electric absorption, for which we employ phabs (Balucinska-Church & McCammon 1992). We find that $\approx$30%, $\approx$8%, and $\approx$3% of the intrinsic flux from H 1743−322 are reduced at 1 keV, 3 keV, and 5 keV by the effects of dust scattering, respectively.[11]

4.2. Modeling Time-averaged Spectra

As noted in Figure 5, the overall spectral shapes in the three epochs are very similar to one another, although the Epoch 2 and Epoch 3 spectra are slightly harder than that of Epoch 1. All of them are roughly characterized by a hard power-law component with a photon index of $\approx$1.6, suggesting that the source is in the low/hard state during the *Suzaku* observations. The hydrogen column density is estimated to be $\approx$2.0 $\times 10^{22}$ cm^{-2} for the photo-electric absorption in cold interstellar medium. This value is well within those obtained in previous studies of H1743−322 (1.6–2.3 $\times 10^{22}$ cm^{-2}; e.g., Capitanio et al. 2009; Miller et al. 2006). A high-energy rollover can be found in 50–100 keV, which is likely to correspond to the electron temperature of the thermal corona. No significant emission and absorption lines can be seen in the spectra.

We first fit the spectra with the nthcomp model (Zdziarski et al. 1996; Życki et al. 1999) with an interstellar absorption. The nthcomp model calculates a thermal Comptonization spectrum parameterized by a photon index, an electron temperature of the Comptonizing corona ($kT_{\rm e}$), and a seed-photon temperature. We could not constrain $kT_{\rm e}$ from a joint fit with the XIS and HXD spectra, due to much poorer statistics of the GSO data compared with those of the XIS that dominate the total χ^2 statistics. We therefore determine $kT_{\rm e}$ only from the GSO spectra,[12] and fix it at the best-fit value in fitting together with the XIS and PIN data. From the joint fit of the XIS + HXD spectra, we obtain χ^2/dof = 1690/1158 (Epoch 1), 1253/994 (Epoch 2), and 1237/904 (Epoch 3), which are far from acceptable. As can be seen in the middle panel in Figure 6, significant residuals remain in the hard X-ray band above 10 keV. A convex-shaped structure can be found, which is likely originated from the reflection of Comptonized photons on the disk.

We next apply a more sophisticated model to the spectra, considering the general picture of the low/hard state. We use the diskbb model (Mitsuda et al. 1984) as the direct emission from the standard disk and the nthcomp model as the Comptonization. The seed photon of the nthcomp component is assumed
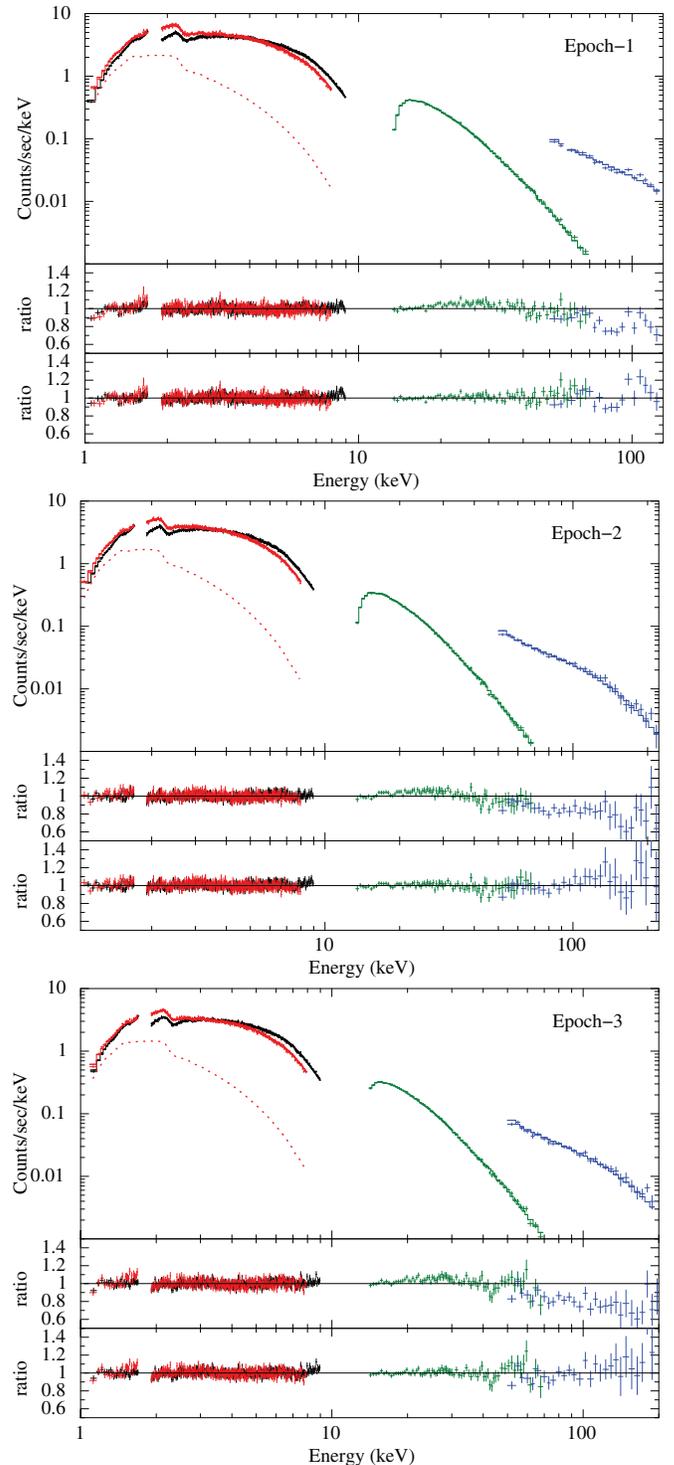

Figure 6. Time-averaged spectra of Epoch 1 (top), Epoch 2 (middle), and Epoch 3 (bottom) fitted with the nthcomp model. The black (below 9 keV), red (below 8 keV), green (14–70 keV), and blue (above 50 keV) points correspond to the XIS-0 + XIS-3, XIS-1, PIN, and GSO data, respectively. The contribution of the scattered flux to the XIS-1 data is shown in red dotted line. The data/model ratio for a single nthcomp model and the final best-fit model are plotted in the second and third panels, respectively.

(A color version of this figure is available in the online journal.)

to be the multi-color disk emission, and the seed temperature is tied to the inner disk temperature of the diskbb component. To account for the reflection component, the ireflect model (Magdziarz & Zdziarski 1995) is convolved to nthcomp.

---

[11] Here $N_{\rm H} = 2 \times 10^{22}$ cm^{-2} is assumed.

[12] Here the seed temperature is fixed at 0.1 keV to constrain $kT_{\rm e}$ so that it does not affect the spectral shape in the GSO band.

This model calculates a reflection spectrum using the ionization parameter ($\xi = L_X/(nR^2)$, where L_X, n, and R are the incident X-ray luminosity, the electron number density, and the distance of reflector from the X-ray source, respectively), the temperature ($T_{\rm disk}$), inclination angle (i), and solid angle ($\Omega/2\pi$) of the reflector. We fix $T_{\rm disk}$ at 30,000 K, which cannot be constrained from the data. The `ireflect` model does not include any emission lines accompanied by the reflection continuum. We thus combine a Gaussian component to account for the iron Kα emission line, which is normally seen in the low/hard state spectra most significantly. Considering numerical studies (e.g., Matt et al. 1991), we link $\Omega/2\pi$ of `ireflect` and the normalization of the Gaussian to keep the equivalent width with respect to the reflection continuum at 1.0 keV. We note that the equivalent width becomes more than an order of magnitude smaller than what is expected in the numerical calculations, when we unlinked the normalization of the Gaussian and the solid angle of `ireflect`. The convolution model `kdblur` (Laor 1991) is also incorporated to model the relativistic blurring by the accretion disk around the black hole. This model uses the index α describing the radial dependence of the emissivity ϵ ($\propto r^{-\alpha}$), inner and outer radii of the accretion disk, and the inclination angle. Here we assume $\alpha = 3$ (i.e., a flat disk) and fix the inner radius at $10R_g$ (where R_g is the gravitational radius, $GM_{\rm BH}/c^2$), and the outer radius at $R_{\rm out} = 400$, which is the maximum value of the `kdblur` model. The integrated fitting model is described as `phabs*Dscat*(diskbb+kdblur*(ireflect*nthcomp [ref]+gauss)+nthcomp[C])`, where `nthcomp[ref]` and `nthcomp[C]` represent the parts of the Comptonized component that is and is not reflected on the disk, respectively. Because `ireflect` and `kdblur` are convolution models, we extend the energy range to 0.01–1000 keV.

The quality of fit is remarkably improved compared with that of the single `nthcomp` model, yielding $\chi^2/{\rm dof} = 1347/1155$ (Epoch 1), 984/991 (Epoch 2), and 995/901 (Epoch 3). The spectra and the best-fit models in the individual epochs are plotted in Figures 6 and 7, respectively. The resultant parameters are given in Table 2. The inclusion of the relativistic blurring model to the reflection component makes a significant statistical improvement ($\Delta\chi^2 = 70$–90, where the degrees of freedom are not changed). When the `kdblur` component is excluded, we obtain $\chi^2/{\rm dof} = 1435/1155$, 1061/991, and 1075/901, for Epochs 1, 2, and 3, respectively. Conversely, the addition of a narrow Gaussian component at 6.4 keV with a 1σ width of 10 eV does not improve the quality of fit.

Assuming an isotropic Comptonized corona and the conservation of the total number of photons from the accretion disk, the inner disk radius can be derived from the formula in Kubota & Makishima (2004):

$$F^p_{\rm disk} + F^p_{\rm thc}2\cos i = 0.0165\left[\frac{r^2_{\rm in}\cos i}{(D/10\ {\rm kpc})^2}\right]\left(\frac{T_{\rm in}}{1\ {\rm keV}}\right)^3$$
$$\times\ {\rm photons\ s^{-1}\ cm^{-2}}, \quad (1)$$

where $F^p_{\rm disk}$ and $F^p_{\rm thc}$ are the 0.01–100 keV photon fluxes of the disk and thermal Comptonized components, respectively. Extending the best-fit model to that energy range, we estimate $F^p_{\rm disk} = 0.699$, 0.646, and 0.489 photons cm^{-2} s^{-1} and $F^p_{\rm thc} = 1.27$, 1.06, and 0.918 photons cm^{-2} s^{-1} in order from Epoch 1 to Epoch 3. The inner disk radii are thus $r_{\rm in} = 101^{+10}_{-9}\ D_{8.5}(\cos i / \cos 75°)^{-1/2}$ km, $r_{\rm in} = 119^{+24}_{-15}\ D_{8.5}(\cos i / \cos 75°)^{-1/2}$ km, and $r_{\rm in} = 92^{+19}_{-10}$
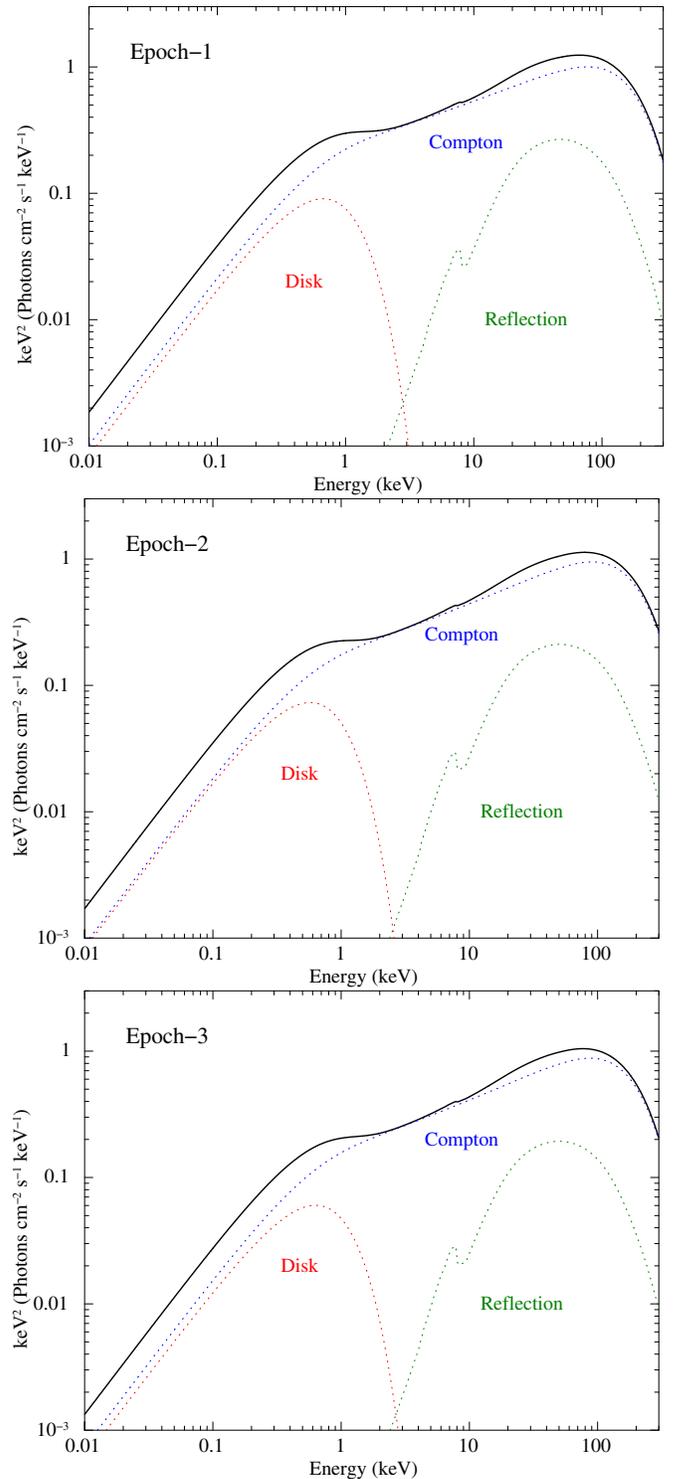

Figure 7. Best-fit models in Epoch 1 (top), Epoch 2 (middle), and Epoch 3 (bottom) plotted in the νF_ν form.
(A color version of this figure is available in the online journal.)

$D_{8.5}(\cos i / \cos 75°)^{-1/2}$ km (where $D_{8.5}$ represents the distance in units of 8.5 kpc). Here we only include the 90% confidence range of the inner disk temperature to estimate the uncertainties of the radii. Multiplying a representative correction factor (1.19) of boundary condition and spectral hardening (Kubota et al. 1998), the actual radii are calculated to be $R_{\rm in} = 120^{+12}_{-11}\ D_{8.5}(\cos i / \cos 75°)^{-1/2}$ km,

Table 2
Best-fit Parameters of the `nthcomp` Model

Component	Parameter	Epoch 1	Epoch 2	Epoch 3
phabs	N_H (10^{22} cm^{-2})	$2.01^{+0.04}_{-0.06}$	1.99 ± 0.04	$1.99^{+0.05}_{-0.06}$
diskbb	kT_{in} (keV)	0.28 ± 0.02	$0.24^{+0.03}_{-0.02}$	$0.27^{+0.02}_{-0.03}$
	Norm	$2.1^{+0.8}_{-1.0} \times 10^3$	$3.1^{+2.7}_{-1.3} \times 10^3$	$1.7^{+1.3}_{-0.8} \times 10^3$
nthcomp	Γ	$1.668^{+0.009}_{-0.005}$	$1.633^{+0.009}_{-0.008}$	1.629 ± 0.009
	kT_e (keV)[a]	<35	68^{+68}_{-20}	61^{+144}_{-21}
	Norm	$0.223^{+0.004}_{-0.006}$	0.174 ± 0.003	0.157 ± 0.004
ireflect	$\Omega/2\pi$	$0.65^{+0.08}_{-0.12}$	0.56 ± 0.07	$0.55^{+0.08}_{-0.07}$
	ξ (erg cm s^{-1})	<6	<31	<68
	T_{disk} (K)	30000 (fixed)	30000 (fixed)	30000 (fixed)
kdblur	α[b]	3 (fixed)	3 (fixed)	3 (fixed)
	R_{in} (R_g)	10 (fixed)	10 (fixed)	10 (fixed)
	R_{out} (R_{out})	400 (fixed)	400 (fixed)	400 (fixed)
	i (deg)	75 (fixed)	75 (fixed)	75 (fixed)
Gauss[c]	E_{cen} (keV)	6.4 (fixed)	6.4 (fixed)	6.4 (fixed)
	σ (keV)	0.01 (fixed)	0.01 (fixed)	0.01 (fixed)
Observed flux	1–10 keV (erg cm^{-2} s^{-1})	9.3×10^{-10}	7.5×10^{-10}	6.9×10^{-10}
Unabsorbed flux[d]	0.01–100 keV (erg cm^{-2} s^{-1})	5.7×10^{-9}	4.8×10^{-9}	4.4×10^{-9}
	χ^2/dof	1347/1155	984/991	995/901

Notes.
[a] The electron temperature is first estimated only from the GSO data and it is fixed at the best-fit value in the joint fit with the XIS and HXD spectra. Although the upper limit for Epoch 1 is not constrained, we adopted the best-estimate value, $kT_e = 57$ keV, in the simultaneous fit.
[b] The emissivity index. The radial dependence of emissivity (ϵ) is expressed with $\epsilon \propto R^{-\alpha}$.
[c] The normalization of the Gaussian is linked to the solid angle of `ireflect` component so that the equivalent width with respect to the reflection continuum is always 1.0 keV.
[d] The flux is corrected for dust scattering.

$R_{in} = 141^{+28}_{-17} D_{8.5}(\cos i / \cos 75°)^{-1/2}$ km, and $R_{in} = 110^{+23}_{-12} D_{8.5}(\cos i / \cos 75°)^{-1/2}$ km for Epochs 1, 2, and 3, respectively.

The inner radius in the high/soft state is $R_{in} = 64 \pm 2 D_{8.5}(\cos i / \cos 75°)^{-1/2}$ km (Chen et al. 2010), which is estimated from the direct disk emission without Comptonization. This value is taken from the first two rows of Table 2 in Chen et al. (2010; which are originally from McClintock et al. 2009 and Capitanio et al. 2009). The fraction of the power-law component in the 2–20 keV flux is less than 6% for these two results and therefore R_{in} is changed by only a few % by including the Comptonized disk photons. The inner radii obtained from the *Suzaku* data are 1.3–2.3 times larger than the value in the high/soft state, suggesting that the standard disk do not extend to the ISCO during the low/hard state observations.

It has been suggested that the Comptonization cloud in the low/hard state has a complex structure. Using *Suzaku* broadband X-ray data, Takahashi et al. (2008), Makishima et al. (2008), Shidatsu et al. (2011b), and Yamada et al. (2013) found that the time-averaged spectra can be described with two Comptonization components that have different optical depths. Moreover, Yamada et al. (2013) detected the second Comptonization component by analyzing the spectral variability. To test the "double Compton" model in the H1743−322 data, we add one more `nthcomp` component and its accompanying reflection component to our final model, and fit the time-averaged spectra. We find, however, that the inclusion of the second Comptonization component does not improve the quality of fit.

4.3. Analysis of Short-term Spectral Variability

We often find it difficult to accurately estimate the cool disk component in the low/hard state by modeling time-averaged spectra, because it is buried in the dominant Comptonized component and coupled with the other structures such as the interstellar absorption and dust scattering. In these cases, the analysis of the short-term spectral variability can be a more powerful approach to separate the disk component. The standard disk and Comptonization in the corona have different properties of spectral variability on the ~1 s timescale; the former generally shows significant variation, while the latter is more stable (e.g., Churazov et al. 2001).

Here we apply "intensity-sorted spectroscopy" described in Makishima et al. (2008) and Yamada et al. (2013) to our *Suzaku* data. Using this technique, Yamada et al. (2013) successfully separated the cool disk component from the highly variable Comptonization in Cyg X-1. We define the high- and low-intensity phases in the same manner as theirs:

$$\{t | C(t) > (1 + f)\overline{C(t)_T}\} \quad (2)$$

and

$$\{t | C(t) < (1 - f)\overline{C(t)_T}\}, \quad (3)$$

respectively, where $C(t)$ is the count rate at the time t for an XIS detector and $\overline{C(t)_T}$ is that averaged over $[t - T/2, t + T/2]$. According to these criteria, we define the time intervals of high- and low-intensity phases using XIS-1 light curves in the 1–10 keV band in 2.0 s binning. We set $f = 0.2$ and $T = 64$ s, so that we obtain both the good photon statistics and a sufficiently high contrast of the intensity between the two phases. The XIS-0 + XIS-3, PIN, and GSO spectra in these two phases are then extracted from the intervals determined by XIS-1. Thus, by using the independent data set for the definition of the time regions, we avoid selection biases merely caused by statistical fluctuation in the photon counts in making the intensity-sorted spectra. A summary of the intensity selection is given in Table 3, and the XIS-1 light curves in the low- and high-intensity phases are presented in Figure 8.
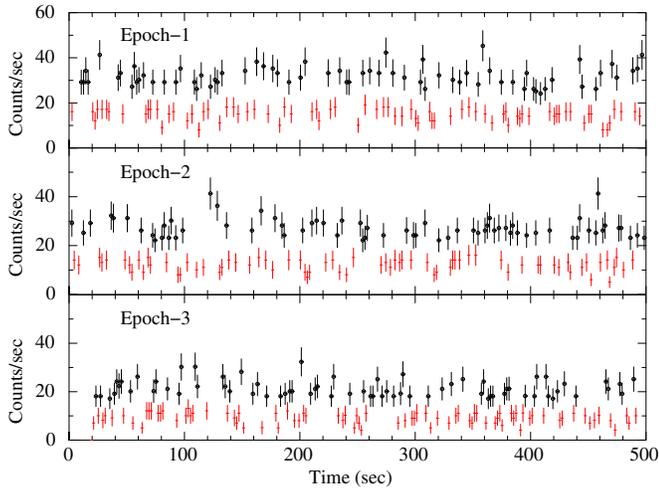
Figure 8. XIS-1 light curves of Epoch 1 (top), Epoch 2 (middle), and Epoch 3 (bottom) in 1–10 keV for the high- (black) and low-intensity (dark gray) phases. The bin size is 2.0 s.

(A color version of this figure is available in the online journal.)

Table 3
Summary of the High- and Low-intensity Selection

	Epoch 1		Epoch 2		Epoch 3	
	High	Low	High	Low	High	Low
Frac. exp. (%)[a]	24	27	24	28	25	29
Ave. rate (count s^{-1})[b]	27	18	22	15	20	14

Notes.
[a] The fraction of time that the source was in the high- and low-intensity phases with respect to the total exposure for each epoch.
[b] Averaged XIS-0 count rates in 1–10 keV.

The high- and low-intensity spectra ($H(E)$ and $L(E)$, respectively) can be separated into the constant component ($d(E)$) and variable components ($h(E)$ and $l(E)$) as

$$H(E) = \omega(E)(d(E) + h(E)) \qquad (4)$$

and

$$L(E) = \omega(E)(d(E) + l(E)), \qquad (5)$$

where $\omega(E)$ represents the photo-electric absorption (which can be regarded as constant on the ~1 s timescale). Unlike Yamada et al. (2013), the constant component $d(E)$ in our data contains not only the direct disk emission but also the scattered-in component, whose short-term variability is smoothed out due to the difference of the light traveling time of each scattered photon. On the other hand, the observed variable component is composed of the Comptonized photons without experiencing dust scattering. For simplicity, we assume the best-fit models obtained from the time-averaged spectra as the scattered-in disk and Comptonization components, and subtract them from both the high- and low-intensity spectra before calculating the spectral ratio $H(E)/L(E)$.

Figure 9 plots the resultant spectral ratio in each epoch. The overall shape is very similar to that of the Cyg X-1 spectra in the low/hard state obtained in Yamada et al. (2013). A turnover below ~2 keV can be seen, suggesting a significant suppression of variability due to the contribution of constant disk component at low energies. The spectral ratios of XIS-0 + XIS-3 without removing the scattered-in component are also presented in pink for comparison. These demonstrate how significantly dust scattering affects the results. We note that the turnover is
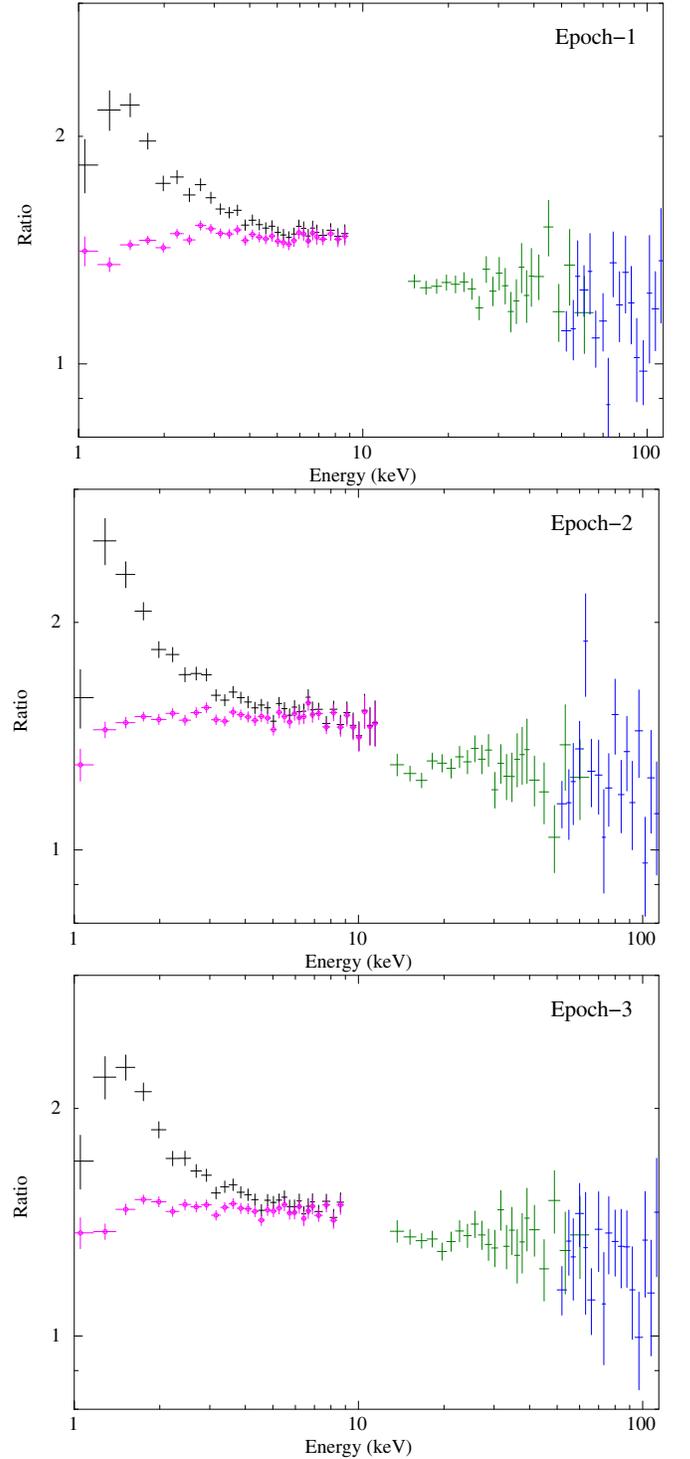

Figure 9. Ratios between the high-intensity and low-intensity spectra in Epoch 1 (top), Epoch 2 (middle), and Epoch 3 (bottom). The ordinate axis in each panel is logarithmically scaled. The scattered-in components are already subtracted from the XIS spectra. The same colors as Figure 6 are used. The XIS-1 data, which are used to determine the intervals of high- and low-intensity phases, are not shown here, because they are affected by Poisson fluctuation of signal counts. The XIS spectral ratio including the scattered-in component is also plotted in pink (open circle).

(A color version of this figure is available in the online journal.)

intrinsic, not generated by the dust scattering. The scattered-in component does not have such a steep turnover, and the decline of variability is seen in the spectral ratio including the scattered-in component as well.

Table 4
Results from the Analysis of Intensity-sorted Spectra

Parameter	Epoch 1	Epoch 2	Epoch 3
$h(E)/l(E)$[a]			
α	2.1 ± 0.1	2.1 ± 0.2	2.0 ± 0.1
β	-0.24 ± 0.06	-0.23 ± 0.06	-0.19 ± 0.06
χ^2/dof	$6.1/6$	$8.1/6$	$13.4/13$
$\omega(E)d(E)$[b]			
N_{H} (10^{22} cm^{-2})	2.0 (fixed)	2.0 (fixed)	2.0 (fixed)
Scatf[c]	0.0 (fixed)	0.0 (fixed)	0.0 (fixed)
T_{in}	$0.22^{+0.40}_{-0.08}$	<0.33	$0.11^{+0.19}_{-0.06}$
Norm	$<8 \times 10^5$	$>2 \times 10^3$	$<1 \times 10^{12}$
χ^2/dof	$3.1/6$	$4.2/3$	$11.3/8$

Notes.
[a] $h(E)/l(E)$ is fitted with αE^{β} in the 2–4 keV band.
[b] $\omega(E)d(E)$, calculated by using the best-fit values of α and β, is fitted with `phabs*Dscat*diskbb`.
[c] The scattering fraction in the `Dscat` model.

Following the procedure of Yamada et al. (2013), we assume that the ratio $H(E)/L(E)$ can be expressed with a single power-law (αE^{β}) in $E > 2$ keV. We determine α and β by fitting the data in the 2–4 keV band (above which they may affected by the reflection component). Using these parameters and Equation (4) and (5), we derive

$$\omega(E)d(E) = \frac{\alpha E^{\beta} L(E) - H(E)}{\alpha E^{\beta} - 1}, \qquad (6)$$

where $d(E)$ is the direct disk spectra. $d(E)$ is then fitted with `phabs*Dscat*diskbb` to estimate the inner temperature and the flux of the constant disk emission. Here the scattering fraction of the `Dscat` model is fixed at 0.0 (i.e., only the effect of scattering out is considered). We assume $N_{\mathrm{H}} = 2.0 \times 10^{22}$ cm^{-2}, which is the averaged value of those determined by the time-averaged spectra in the individual epochs. However, the parameters are only very weakly constrained due to the poor statistics in the soft X-ray band around the turnover of the spectral ratios, although the values are consistent with those estimated from the time-averaged spectra. The fitting parameters are summarized in Table 4.

5. NEAR-INFRARED AND OPTICAL OBSERVATIONS AND THE RESULTS

In addition to the X-ray observations with *Suzaku*, we performed infrared photometric observations of H1743−322 in the J (1.25 μm), H (1.63 μm), and K_s (2.14 μm) bands, with the SIRIUS camera (Nagayama et al. 2003) on the 1.4m *IRSF* telescope at the South African Astronomical Observatory during the 2012 outburst. Optical observations through R_C and I_C filters were also carried out by using Hiroshima One-shot Wide-field Polarimeter (HOWPoI; Kawabata et al. 2008) attached to the 1.5 m *Kanata* telescope at Higashi-Hiroshima Observatory. The counterpart of H1743−322 was not detected in any bands, however. The typical seeing was $\approx 1''.8$ for the *IRSF* J band and $2''.3$ for the *Kanata* R_C band in FWHM.

In the analysis of the *IRSF* data, we combine all the frames taken in one night and perform dark-subtraction, flat-fielding, sky-subtraction, and combining the dithered images using the SIRIUS pipeline software running on Image Reduction and Analysis Facilities (IRAF; Tody 1986) version 2.16. H1743−322 is located in a crowded region close to the Galactic
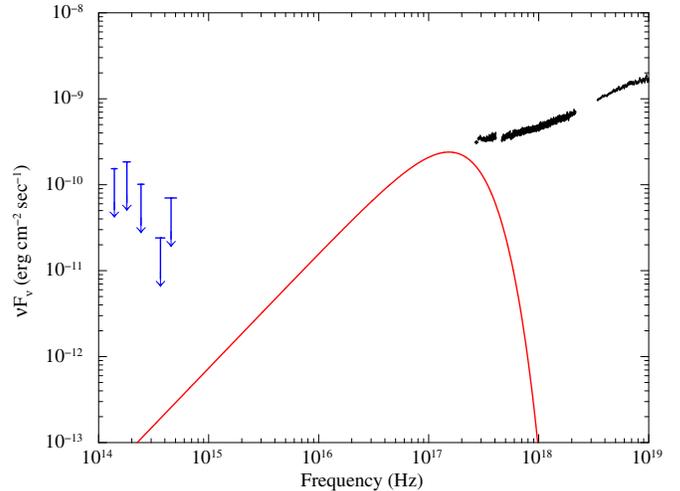

Figure 10. Spectral energy distribution of H1743−322 on 2012 October 12. The upper limits in the extinction-corrected optical (R_C and I_C) and near-infrared (J, H, and K_S bands) fluxes are plotted in blue arrows. The black points are the *Suzaku* spectra, corrected for neutral absorption and dust scattering. Red solid line shows the intrinsic disk emission including the Comptonized photons, where the outer disk is assumed to extend to infinity.
(A color version of this figure is available in the online journal.)

center, and the near-infrared counterpart in the *IRSF* images is buried in nearby bright sources. We estimate the upper flux in each band from the counts on the pixel at the position of H1743−322. Count-flux conversion is made by comparison with the stellar photometry of nearby sources with the Two Micron All Sky Survey magnitude (Skrutskie et al. 2006). We reduce the *Kanata* data in a standard way for the aperture photometry of optical CCD data. The upper magnitudes in the R_C and I_C bands are determined by the detection limits of a point source in the image, estimated from the background level of source-free regions near H1743−322.

Figure 10 presents the upper limits of the optical and near-infrared fluxes on 2012 October 12, together with the contemporaneous *Suzaku* spectrum (in Epoch 3). The flux limits in the optical and near-infrared bands are corrected for the Galactic extinction. Substituting the hydrogen column density of H1743−322 ($N_{\mathrm{H}} \approx 2 \times 10^{22}$ cm^{-2}) into the N_{H} versus A_{V} relation (where A_{V} represents the extinction in the V band; Predehl & Schmitt 1995), we derive $A_{\mathrm{V}} \approx 11$. We convert A_{V} to the extinction in the R_C, I_C, J, H, and K_S bands using the extinction curve for $R_{\mathrm{V}} = 3.1$ given by Cardelli et al. (1989). The upper limits of the extinction-corrected absolute R_C, I_C, J, H, and K_S magnitudes are estimated to be -1.9, -0.5, -3.8, -5.2, and -5.8, respectively. We find that if the companion is a main sequence star, it should be a late-B or a less massive star (Wainscoat et al. 1992).

The upper limits are consistent with the intrinsic disk flux including the Compton-scattered photons (shown in red in Figure 10), and with the possible contribution of the synchrotron emission from the compact jet. If the positive relation between radio and X-ray fluxes found by Coriat et al. (2011) holds in the 2012 outburst, the *Suzaku* flux in Epoch 3 (5.2×10^{-10} erg cm^{-2} s^{-1} in the 3–9 keV band) corresponds to 0.68 mJy at 8.5 GHz flux. Assuming that the flat optically thick synchrotron spectrum extends up to the optical bands, we estimate the jet contribution to be $\nu F_\nu \approx 4 \times 10^{-12}$ erg cm^{-2} s^{-1} at 5×10^{14} Hz. This is more than ≈ 10 times lower than the optical and near-infrared upper flux limits.

6. DISCUSSION

6.1. Failed Outburst in 2012 October

We observed H1743−322 with *Suzaku* at the flux peak and early decaying phase during the outburst in 2012 September and October. The time-averaged spectra in all the three epochs are approximated by a power-law with a photon index of ≈1.6, which is well within the typical values in the low/hard state (1.5–2.0; e.g., Done et al. 2007). The PIN power spectra in the 14–70 keV band show strong variability above ≈0.1 Hz with a power of 1×10^{-2} (rms²/Hz²), which most likely corresponds to the flat part of the band-limited noise. These X-ray spectral and timing properties support that the source was in the low/hard state during the *Suzaku* observations.

As noted in Figure 1, the long-term *MAXI* data do not show significant softening around the peak flux. This suggests that the state transition from the low/hard state to the high/soft state (hard-to-soft transition) did not occur in the late 2012 outburst. This type of outburst is often classified as a "failed outburst," which exhibits no hard-to-soft transition or an incomplete transition only reaching the intermediate state. A few failed outbursts have been reported in H1743−322 so far (Capitanio et al. 2009; Chen et al. 2010). In addition to this source, there are a few other BHXBs that underwent failed outbursts, like XTE J1550−564 and MAXI J1836−164 (Sturner & Shrader 2005; Ferrigno et al. 2012). The 1–500 keV unabsorbed luminosity in Epoch 1 (calculated from the best-fit model) is estimated to be $6.1 \times 10^{37} D_{8.5}^2$ erg s⁻¹. This is a few times lower than the luminosity at which H1743−322 generally makes a hard-to-soft transition (e.g., McClintock et al. 2009; Zhou et al. 2013), suggesting that the mass accretion rate was not enough to trigger a transition.

6.2. Structure of Inner Disk and Corona

The time-averaged *Suzaku* spectra are well described with thermal emission from the standard disk, its Comptonized emission by a hot corona, and the reflection component from the accretion disk. The overall spectral shape is not largely changed in the three epochs, while the 2–20 keV fluxes in Epoch 2 and Epoch 3 are ≈20% lower than that in Epoch 1. Although the inner disk temperature and the photon index of the Comptonization decrease by 10%–30% and 0.03 from Epoch 1 to the latter two epochs, the other parameters remain the same within their 90% confidence ranges. We find that the double Comptonization model is not necessary to reproduce the spectra. The same was suggested with the *Suzaku* spectrum of MAXI J1305−704 in the low/hard state at $\sim 0.01 L_{\mathrm{Edd}}$ (Shidatsu et al. 2013). In the case of Cyg X-1, the softer Comptonization component is more clearly seen in the brighter low/hard (or hard intermediate) states (Yamada et al. 2013). Thus, the luminosities of H1743−322 in the *Suzaku* observations ($\approx 0.04 \, D_{8.5}^2 M_{10}^{-1} L_{\mathrm{Edd}}$ in the 1–500 keV band) may not be sufficiently high to detect the softer Comptonization component significantly.

As noted in Figure 5, the GSO spectra suggest the evidence of the high-energy rollover around 50–100 keV, likely correspond to the electron temperature of the Comptonized corona. From the spectral fit with the GSO data, the electron temperature is estimated to be $kT_{\mathrm{e}} \approx 60$ keV. We note, however, that the value may be somewhat overestimated because the `nthcomp` model does not include relativistic effects properly; its output spectrum drops more sharply above the rollover than the that of the real Comptonization spectrum (see Done 2010). Previous observations of H1743−322 with *INTEGRAL* and *Suzaku*

at similar luminosities reported the detection of the cutoff energy (e.g., Capitanio et al. 2005; Blum et al. 2010). The anti-correlation between the electron temperature and the X-ray luminosity in the bright ($\lesssim 0.1 L_{\mathrm{Edd}}$) low/hard state was suggested by Miyakawa et al. (2008) with the *Rossi X-ray Timing Explorer* (*RXTE*; Bradt et al. 1993) spectra of GX 339−4. Chiang et al. (2010) also found in the *RXTE* data of Swift J1753.5−0127 that the electron temperature is relatively low in the bright low/hard state like in our case, and that it moves to higher energies in accordance with the decline of an outburst. It would be explained if inverse Compton cooling in the corona is more efficient by a relatively higher input rate of seed photons in brighter periods (Miyakawa et al. 2008).

We find that the X-ray spectra are dominated by the Comptonized component and that the direct disk emission is very weak in the *Suzaku* bandpass. The disk temperature estimated from the time-averaged spectra is much smaller than typical values in the high/soft state (≈1 keV; e.g., McClintock & Remillard 2006). We calculate the inner disk radius from the intrinsic disk flux including the disk photons consumed by Compton-scattering in the corona in each epoch. The radii are found to be 1.3–2.3 times larger than that in the high/soft state, supporting the idea that the standard disk does not extend to the ISCO in the low/hard state. This is consistent with the somewhat smaller solid angle of the reflection component than those obtained in the very high state by using similar spectral models (Tamura et al. 2012; Hori et al. 2014).

We note, however, the calculated inner radii should be taken with caution, since this is somewhat dependent on spectral modeling. We considered only the statistical uncertainties of the inner disk temperatures, but additional errors may be produced in modeling the effects of dust scattering. Also, the spectral hardening factor of disk emission for deriving the actual inner radii could be different between the high/soft and low/hard states (e.g., Shimura & Takahara 1995). Moreover, we assumed that all the seed photons originated from the disk, but if other emission components contribute, the inner radii could become smaller. For more precise estimation of the inner disk radii, we have to assess these possible uncertainties thoroughly by using higher-quality wide-band spectra, particularly from the sources with a much smaller absorption column. This is left for future work.

We successfully detect the weak, cool disk component independently of the time-averaged spectral modeling, using the spectral variability on a short (≈1 s) timescale. The overall profile of spectral ratio between high- and low-intensity phases is very similar to what Yamada et al. (2013) found in Cyg X-1 data during the low/hard state. The power of short-term variability clearly declines below 1–2 keV, suggesting that the constant standard disk component contributes to the soft X-ray flux. Modeling the profile of the spectral ratio in the same manner as Yamada et al. (2013), we estimate the inner radius and temperature of the disk component. Although the resultant parameters have large uncertainties due to poor statistics, they are consistent with those obtained from the time-averaged spectra.

The mass accretion rate of the disk can be derived through $L_{\mathrm{disk}} = G M_{\mathrm{BH}} \dot{m}_{\mathrm{disk}}/(2R_{\mathrm{in}})$, where L_{disk} and $\dot{m}_{\mathrm{disk}}$ represent the luminosity and mass accretion rate of the disk component, respectively. We estimate $L_{\mathrm{disk}} = 2.5 \times 10^{36} \, D_{8.5}^2$ erg s⁻¹ (the unabsorbed disk luminosity in the 0.01–500 keV band) and $R_{\mathrm{in}} = 120 \, D_{8.5}(\cos i \,/ \cos 75°)^{-1/2}$ km (for Epoch 1) and thus we have $\dot{m}_{\mathrm{disk}} = 4.5 \times 10^{16} D_{8.5}^3 \, M_{10}^{-1}(\cos i \,/ \cos 75°)^{-1/2}$ g s⁻¹. The accretion rate of corona can be calculated as $L_{\mathrm{c}} = \eta \dot{m}_{\mathrm{c}} c^2$,

where η, L_c, and $\dot{m}_c$ are the radiative efficiency, the luminosity, and the mass accretion rate of the corona, respectively. Using the best-fit `nthcomp` component for Epoch 1 as L_c (5.1×10^{37} $D_{8.5}^2$ erg s^{-1}), we obtain $\dot{m}_c = 5.7 \times 10^{17}$ $D_{8.5}$ g s^{-1} if the corona is radiatively efficient ($\eta = 0.1$ is assumed). It can be much larger in the case of a radiatively inefficient flow. Thus, $\dot{m}_c$ is much larger than $\dot{m}_{disk}$, regardless of the radiative efficiency. This is inconsistent with the simple truncation disk model, in which the standard disk makes transition at the truncated radius into the hot inner flow with the same mass accretion rate.

A possible explanation is that there may be a separate coronal accretion flow with a large-scale height extending from the outer edge of the disk to the black hole, and that its mass accretion rate is much larger than that of the thin disk. There is another possibility, which reconciles the mass accretion rates of the disk and corona. If the soft X-ray component is not the disk itself, but is instead originated from a much smaller, hot clumps torn off the inner edge of a much larger disk (Chiang et al. 2010; Yamada et al. 2013), the true disk component has larger normalization but is truncated at a larger radius. In this case, $\dot{m}_{disk}$ can be comparable to $\dot{m}_c$, and the true inner disk temperature can be much lower, making impossible to detect the disk component in the soft X-ray bandpass. The cool disk component peaking in the EUV band was actually detected in a low/hard state spectrum of XTE J1118 + 480 (Esin et al. 2001), along with a much smaller soft X-ray component (Reis et al. 2009), which would be from the clumps (Chiang et al. 2010).

6.3. Ionized Absorber and Disk Wind

Miller et al. (2006) discovered blueshifted, ionized absorption lines at 6.7 keV and 7.0 keV (corresponding to He-like and H-like iron Kα lines, respectively) in the *Chandra* high-resolution spectra of H1743−322 in the high/soft and very high (or soft intermediate) states. These lines, often seen in high inclination sources (e.g., Ueda et al. 1998; Kotani et al. 2000; Lee et al. 2002), likely originated from the disk wind. They show "state-dependent" behavior and are rarely detected in the low/hard state (e.g., Neilsen & Lee 2009; Ponti et al. 2012). For H 1743−322, the non-detection of the iron absorption lines in the low/hard state was previously reported by Blum et al. (2010) and Miller et al. (2012).

Our *Suzaku* data do not exhibit any significant absorption features apparently. To check the presence of the ionized iron absorption lines, we add two negative Gaussian components to the best-fit model for the time-averaged spectra. Here we assume a wind velocity of 300 km s^{-1} and a 1σ line width of 20 eV (which can be regarded as representative values of Miller et al. 2006) and fix all the parameter except for the normalizations of continuum and line components. We estimate the 90% upper limits of the equivalent widths in Epoch 2 to be 22 eV for both H-like and He-like iron lines, which are similar or slightly larger values than those obtained in Miller et al. (2006). Thus, we cannot exclude the presence or disappearance of the ionized iron absorption lines.

6.4. Origin of QPO

A weak LF QPO is detected at 0.1–0.2 Hz in each epoch. We find that the QPO frequency becomes $\approx$30% lower in accordance with the $\approx$20% decrease of the hard X-ray luminosity in the 15–50 keV band. LF QPOs (below 10 Hz) were detected in many BHXBs during the low/hard and intermediate states, such as XTE J150−564 (e.g., Cui et al. 1999; Sobczak et al. 1999)

and GX 339−4 (e.g., Miyamoto et al. 1991; Motta et al. 2011; Tamura et al. 2012). Previous studies suggested that their frequencies are positively correlated with the photon index of the Comptonization below $\approx$10 Hz, at which the correlation saturates (Vignarca et al. 2003; Titarchuk & Fiorito 2004; Titarchuk & Shaposhnikov 2005). Our results follow this ubiquitous correlation between the QPO frequency and the photon index; the photon index becomes lower by $\approx$0.03 in the $\approx$30% decrease of the QPO frequency.

The correlations of the observed LF-QPO frequencies with the X-ray flux and the photon index lead us to invoke the idea that they are associated with the inner disk structure. Ingram et al. (2009) suggested the possibility that the LF QPOs of BHXBs are produced by the Lense–Thirring precession of the hot inner flow extended between the black hole and the inner edge of the disk. Their model can describe both the QPO frequencies and the observed X-ray spectrum, and predicts the anti-correlation with the inner disk radius and the QPO frequency. In the truncation disk model, the inner radius recedes as the mass accretion rate is decreased (see Done et al. 2007). At the same time, the power of seed photons illuminating the hot flow becomes weaker, making the observed X-ray spectrum harder. The decrease of the LF-QPO frequency can be explained if it reflects the timescale at the inner radius, where the standard disk is replaced to the hot flow (Ingram et al. 2009). Axelsson et al. (2014) extracted the spectrum of the pure QPO component from the *RXTE* data of XTE J1550−564 and found that it can indeed be interpreted by the Comptonization in the hot inner flow. Although the inner disk radii that we estimated from the *Suzaku* data in each epoch have large uncertainties, they are compatible to the anti-correlation trend between the QPO frequency and the inner disk.

The QPO frequencies correspond to 40–50 R_g in the Lense–Thirring precession model of Ingram et al. (2009), if a black hole mass of $10M_\odot$ is assumed. This is about several to 10 times larger than what we estimated from the time-averaged spectra. The possible reason of this inconsistency would be that the QPO was generated by a more complicated mechanism, or that we are underestimating the true inner disk radius, as is also suggested in Section 6.2 by assuming that the mass accretion rate through the disk and that in the coronal flow are the same. A separate, small variable soft component could simultaneously allow the QPO to be consistent with a Lense–Thirring origin, and for the corona to be fed directly by the mass accreting through the disk.

7. SUMMARY AND CONCLUSION

We observed the black hole transient H 1743−322 with *Suzaku* on three occasions during the outburst in 2010 October, which provided one of the best quality broad band X-ray spectra of this source in the low/hard state. The results are summarized as follows.

1. We find that the observed X-ray spectra are significantly affected by dust scattering in the interstellar medium with $N_H \approx 2 \times 10^{22}$ cm^{-2}, which must be corrected for accurate spectral analyses.
2. The time-averaged spectra are dominated by a strong Comptonization in the corona with an electron temperature of $\approx$60 keV. The disk reflection component with $\Omega/2\pi \approx 0.6$ is detected. The estimated inner disk radius is larger than that in the high/soft state, suggesting that the standard disk is truncated at 1.3–2.3 times larger radii than the ISCO during the *Suzaku* observations.

3. We estimate the cool disk component by investigating short-term spectral variability on the $\sim$1 s timescale, independently of the time-averaged spectral modeling. We find that the spectral ratio between the high- and low-intensity phases has a very similar shape to those of Cyg X-1 in the low/hard state, indicating the presence of stable disk emission at low energies.

4. A weak LF QPO was detected at 0.1–0.2 Hz. We find that the QPO frequency becomes lower as the X-ray luminosity and photon index decrease. This may be explained by the evolution of the disk truncation radius.

REFERENCES

Anders, E., & Grevesse, N. 1989, GeCoA, 53, 197
Axelsson, M., Borgonovo, L., & Larsson, S. 2005, A&A, 438, 999
Axelsson, M., Done, C., & Hjalmarsdotter, L. 2014, MNRAS, 438, 657
Baba, D., Nagata, T., Iwata, I., et al. 2003, IAU Circ., 8112, 2
Balucinska-Church, M., & McCammon, D. 1992, ApJ, 400, 699
Barthelmy, S. D., Barbier, L. M., Cummings, J. R., et al. 2005, SSRv, 120, 143
Baumgartner, W. H., Tueller, J., Markwardt, C. B., et al. 2013, ApJS, 207, 19
Blum, J. L., Miller, J. M., Cackett, E., et al. 2010, ApJ, 713, 1244
Bradt, H. V., Rothschild, R. E., & Swank, J. H. 1993, A&AS, 97, 355
Capitanio, F., Belloni, T., Del Santo, M., et al. 2009, MNRAS, 398, 1194
Capitanio, F., Ubertini, P., Bazzano, A., et al. 2005, ApJ, 622, 503
Cardelli, J. A., Clayton, G. C., & Mathis, J. S. 1989, ApJ, 345, 245
Chiang, C. Y., Done, C., Still, M., & Godet, O. 2010, MNRAS, 403, 1102
Chen, Y. P., Zhang, S., Torres, D. F., et al. 2010, A&A, 522, 99
Churazov, E., Gilfanov, M., & Revnivtsev, M. 2001, MNRAS, 321, 759
Corbel, S., Kaaret, P., Fender, R. P., et al. 2005, ApJ, 632, 504
Coriat, M., Corbel, S., Prat, L., et al. 2011, MNRAS, 414, 677
Cui, W., Zhang, S. N., Chen, W., & Morgan, E. H. 1999, ApJL, 512, L43
Done, C. 2010, arXiv:1008.2287
Done, C., Gierliński, M., & Kubota, A. 2007, A&ARv, 15, 1
Draine, B. T. 2003, ApJ, 598, 1026
Ebisawa, K., Makino, F., & Mitsuda, K. 1993, ApJ, 403, 684
Esin, A. A., McClintock, J. E., Drake, J. J., et al. 2001, ApJ, 555, 483
Ferrigno, C., Bozzo, E., Del Santo, M., et al. 2012, A&A, 537, L7
Fukazawa, Y., Mizuno, T., Watanabe, S., et al. 2009, PASJ, 61, 17
Homan, J., Miller, J. M., Wijnands, R., et al. 2003, ATel, 162, 1
Homan, J., Miller, J. M., Wijnands, R., et al. 2005, ApJ, 623, 383
Hori, T., Ueda, Y., Shidatsu, M., et al. 2014, ApJ, in press
Ingram, A., & Done, C. 2012, MNRAS, 419, 2369
Ingram, A., Done, C., & Fragile, P. C. 2009, MNRAS, 397, L101
Ishisaki, Y., Maeda, Y., Fujimoto, R., et al. 2007, PASJ, 59, 113
Kaluzienski, L. J., & Holt, S. S. 1977, IAU Circ. 3099, 3
Kawabata, K. S., Nagae, O., Chiyonobu, S., et al. 2008, Proc. SPIE, 7014, 151
Kolehmainen, M., Done, C., & Diaz Trigo, M. 2014, MNRAS, 437, 316
Kotani, T., Ebisawa, K., Dotani, T., et al. 2000, ApJ, 539, 413
Krivonos, R., Revnivtsev, M., Churazov, E., et al. 2007, A&A, 463, 957
Kubota, A., & Makishima, K. 2004, ApJ, 601, 428
Kubota, K., Ueda, Y., Kawai, N., et al. 2010, PASJ, 62, 323
Kubota, A., Tanaka, Y., Makishima, K., et al. 1998, PASJ, 50, 667
Laor, A. 1991, ApJ, 376, 90
Lee, J. C., Reynolds, C. S., Remillard, R., et al. 2002, ApJ, 567, 1102
Magdziarz, P., & Zdziarski, A. A. 1995, MNRAS, 273, 837
Makishima, K., Takahashi, H., Yamada, S., et al. 2008, PASJ, 60, 585
Matsuoka, M., Kawasaki, K., Ueno, S., et al. 2009, PASJ, 61, 999
Matt, G., Perola, G. C., & Piro, L. 1991, A&A, 247, 25
McClintock, J. E., & Remillard, R. A. 2006, in Compact Stellar X-Ray Sources, ed. W. H. G. Lewin & M. van der Klis (Cambridge: Cambridge Univ. Press), 157
McClintock, J. E., Remillard, R. A., Rupen, M. P., et al. 2009, ApJ, 698, 1398
Mihara, T., Nakajima, M., Sugizaki, M., et al. 2011, PASJ, 63, 623
Miller, J. M., Raymond, J., Fabian, A. C., et al. 2012, ApJL, 759, L6
Miller, J. M., Raymond, J., Homan, J., et al. 2006, ApJ, 646, 394
Mitsuda, K., Bautz, M., Inoue, H., et al. 2007, PASJ, 59, 1
Mitsuda, K., Inoue, H., Koyama, K., et al. 1984, PASJ, 36, 741
Miyamoto, S., Kimura, K., Kitamoto, S., et al. 1991, ApJ, 383, 784
Miyakawa, T., Yamaoka, K., Homan, J., et al. 2008, PASJ, 60, 637
Motta, S., Muñoz-Darias, T., Casella, P., et al. 2011, MNRAS, 418, 2292
Nagayama, T., Nagashima, C., Nakajima, Y., et al. 2003, Proc. SPIE, 4841, 459
Neilsen, J., & Lee, J. C. 2009, Natur, 458, 481
Ponti, G., Fender, R. P., Begelman, M. C., et al. 2012, MNRAS, 422, L11
Predehl, P., & Schmitt, J. H. M. M. 1995, A&A, 293, 889
Reis, R. C., Miller, J. M., & Fabian, A. C. 2009, MNRAS, 395, L52
Rupen, M. P., Mioduszewski, A. J., & Dhawan, V. 2003, ATel, 142
Shaposhnikov, N., & Titarchuk, L. 2007, ApJ, 663, 445
Shakura, N. I., & Sunyaev, R. A. 1973, A&A, 24, 337
Shidatsu, M., Negoro, H., Nakahira, S., et al. 2012, ATel, 4419
Shidatsu, M., Ueda, Y., Nakahira, S., et al. 2011a, PASJ, 63, 803
Shidatsu, M., Ueda, Y., Nakahira, S., et al. 2013, ApJ, 779, 26
Shidatsu, M., Ueda, Y., Tazaki, F., et al. 2011b, PASJ, 63, 785
Shimura, T., & Takahara, F. 1995, ApJ, 445, 780
Skrutskie, M. F., Cutri, R. M., Stiening, R., et al. 2006, AJ, 131, 1163
Smith, R. K., Edgar, R. J., & Shafer, R. A. 2002, ApJ, 581, 562
Sobczak, G. J., McClintock, J. E., Remillard, R. A., et al. 1999, ApJL, 517, L121
Sobczak, G. J., McClintock, J. E., Remillard, R. A., et al. 2000, ApJ, 531, 537
Steeghs, D., Miller, J. M., Kaplan, D., et al. 2003, ATel, 146
Steiner, J. F., McClintock, J. E., & Reid, M. J. 2012, ApJL, 745, L7
Steiner, J. F., McClintock, J. E., Remillard, R. A., et al. 2010, ApJL, 718, L117
Sturner, S. J., & Shrader, C. R. 2005, ApJ, 625, 923
Takahashi, T., Abe, K., Endo, M., et al. 2007, PASJ, 59, 35
Takahashi, H., Fukazawa, Y., Mizuno, T., et al. 2008, PASJ, 60, 69
Tamura, M., Kubota, A., Yamada, S., et al. 2012, ApJ, 753, 65
Tanaka, Y., & Shibazaki, N. 1996, ARA&A, 34, 607
Titarchuk, L., & Fiorito, R. 2004, ApJ, 612, 988
Titarchuk, L., & Shaposhnikov, N. 2005, ApJ, 626, 298
Tody, D. 1986, Proc. SPIE, 627, 733
Tomsick, J. A., & Kalemci, E. 2003, ATel, 198
Tomsick, J. A., Yamaoka, K., Corbel, S., et al. 2009, ApJL, 707, L87
Ueda, Y., Honda, K., Takahashi, H., et al. 2010, ApJ, 713, 257
Ueda, Y., Inoue, H., Tanaka, Y., et al. 1998, ApJ, 492, 782
Vignarca, F., Migliari, S., Belloni, T., et al. 2003, A&A, 397, 729
Wainscoat, R. J., Cohen, M., Volk, K., Walker, H. J., & Schwartz, D. E. 1992, ApJS, 83, 111
Yamada, S., Makishima, K., Done, S., et al. 2013, PASJ, 65, 80
Yamada, S., Uchiyama, H., Dotani, T., et al. 2012, PASJ, 64, 53
Zdziarski, A. A., Johnson, W. N., & Magdziarz, P. 1996, MNRAS, 283, 193
Zhou, J. N., Liu, Q. Z., Chen, Y. P., et al. 2013, MNRAS, 431, 2285
Życki, P. T., Done, C., & Smith, D. A. 1999, MNRAS, 309, 561